



The Deflection of the Cartwheel CME: ForeCAT Results

Luisa Capannolo¹, Merav Opher¹, Christina Kay², and Enrico Landi³

¹ Boston University, Boston, MA 02215, USA; luisacap@bu.edu

² Solar Physics Laboratory, NASA Goddard Space Flight Center, Greenbelt, MD 20771, USA

³ University of Michigan, Ann Arbor, MI 48109, USA

Received 2017 February 16; revised 2017 March 26; accepted 2017 March 27; published 2017 April 12

Abstract

We analyze the Cartwheel coronal mass ejection's (CME; 2008 April 9) trajectory in the low corona with the ForeCAT model. This complex event presented a significant rotation in the low corona and a reversal in its original latitude direction. We successfully reproduce the observed CME's trajectory (latitude and longitude deflection) and speed. Through a χ^2 test, we are able to constrain the CME's mass to $(2.3\text{--}3.0) \times 10^{14}$ g and the CME's initial shape. We are able to constrain the expansion of the CME as well: the angular width linearly increases until $2.1 R_{\odot}$, and is constant afterward. In order to match the observed latitude, we include a non-radial initial speed of -42 km s^{-1} . Despite allowing the CME to rotate in the model, the magnetic forces of the solar background are not able to reproduce the observed rotation. We suggest that the complex reversal in latitude and the significant rotation of the Cartwheel CME can be justified with an asymmetrical reconnection event that ejected the CME non-radially and also initiated its rotation.

Key words: Sun: coronal mass ejections (CMEs)

1. Introduction

Coronal mass ejections (CMEs) are explosions of a significant amount (on average $10^{14}\text{--}10^{16}$ g) of magnetized solar plasma over timescales of minutes or hours. CMEs have energies of up to 10^{33} erg and propagate with speeds that can span from 50 to 2500 km s^{-1} (Gopalswamy et al. 2009b). Being magnetic structures propagating outward, CMEs are of high scientific interest because the embedded magnetic field can interact with the terrestrial magnetosphere. CMEs, in fact, represent one of the major causes of geomagnetic activity at Earth (Gosling et al. 1991; Gosling 1993). The possible on-set of geomagnetic storms directly affects satellite performance and power grid reliability, as well as endangers the health of astronauts and high-latitude route airplane passengers. Predicting the time of CME arrival at Earth's magnetosphere and its parameters (speed, magnetic field, etc.) is therefore fundamental in the space weather community.

Rather than traveling radially, CMEs often show more complex trajectories. As the CME propagates, its latitude and longitude can vary from a straight radial path (Hildner 1977; MacQueen et al. 1986; Isavnin et al. 2014). Since the CME trajectory might be affected by latitude and longitude deflection, knowing only the location of the ejection on the Sun's surface is not sufficient to predict the CME position far from the Sun. A potentially innocuous CME, not originally directed toward Earth, might become geomagnetically significant if its trajectory is altered such that it intercepts the terrestrial magnetosphere. An example of this is offered by the 2008 December 10 CME, which deflected more than 30° , from high latitude to the solar equator (Byrne et al. 2010). On the other hand, significant deflection might prevent the impact of Earth-directed CMEs (Mays et al. 2015; Möstl et al. 2015). Since deflection plays such an important role, modeling CME trajectories is crucial to predict if a CME will impact Earth's magnetosphere.

Observations (Green et al. 2007; Vourlidas et al. 2011; Thompson et al. 2012; Isavnin et al. 2014) and simulations (Lynch et al. 2009; Kliem et al. 2012) have also shown that

CMEs can rotate while they propagate outward. Under these circumstances, the orientation of the magnetic field embedded in these structures changes. The strength and orientation of an impacting CME's magnetic field is directly related to the strength of the geomagnetic storm it may cause. As a result, space weather predictions should also take into account the rotation a CME undergoes during its propagation from the Sun to the Earth.

Forecasting a Coronal Mass Ejection's Altered Trajectory (ForeCAT—Kay et al. 2013, 2015b) is a model that predicts the CME trajectory as a function of radial distance from the Sun: the CME deflection in latitude and/or in longitude is calculated considering magnetic forces (tension and pressure gradient) from the solar background. CME deflection governed by background magnetic forces is widely accepted in the community (Gopalswamy et al. 2009a; Gui et al. 2011; Shen et al. 2011). ForeCAT uses the Potential Field Source Surface (PFSS) model for the magnetic background: the solar magnetic field is reconstructed from a synoptic magnetogram, assuming that no currents exist within the source surface radius (R_{SS}). We run simulations with $R_{SS} = 2.5 R_{\odot}$ because it is the value commonly used in the literature (Luhmann et al. 2002). Future work will use other solar wind background models for comparison, such as the Current Sheet Source Surface (CSSS) model (developed in Zhao & Hoeksema 1995), which considers sheet and volume currents in the low corona as well. ForeCAT also includes CME rotation due to the torque resulting from possibly unbalanced magnetic forces acting on different points of the flux rope.

ForeCAT input parameters include the initial CME mass, speed, size and shape, and location. When observational data close to the Sun's surface are available, these parameters are data-constrained, otherwise they are treated as free parameters and later constrained by simulation-data comparisons. Once the ForeCAT input parameters are fixed, the model predicts the full CME trajectory (deflection, rotation, speed) based on the driving magnetic forces from the solar background (Kay et al. 2013, 2015b, 2016).

From previous works, CME trajectories are deflected mainly in the low corona (until $\sim 5 R_{\odot}$), where the magnetic gradients are the strongest (Kay et al. 2013, 2015b). In agreement with the literature, CME trajectories simulated with ForeCAT deflect toward the heliospheric current sheet (HCS) and away from coronal holes (Cremades & Bothmer 2004; Gopalswamy et al. 2009a; Kilpua et al. 2009).

By comparing the simulation outputs to available data (CME position and speed as functions of radial distance in the solar corona), ForeCAT not only constrains the CME free parameters, but also provides information on the CME expansion (Kay et al. 2016). A ForeCAT simulation is computationally very inexpensive and fast (one run is generally under ~ 1 – 2 minutes using GPU on an average Ubuntu machine) as compared to MHD ones (which can take days to complete on supercomputers), making this model a good future candidate for a real-time space weather tool.

ForeCAT has successfully matched several observed CME trajectories (Kay et al. 2015a, 2016, 2017). Here, we explore a more complex CME, ejected on 2008 April 9 (during solar minimum of cycle 24) at 9:25 UT. This CME is referred to as the “Cartwheel CME” due to its unusual latitudinal motion and complex rotation, very different than the previous simpler cases of CMEs analyzed with ForeCAT. Because of its complexity, the Cartwheel CME has been widely studied in the literature (Landi et al. 2010; Savage et al. 2010; Gui et al. 2011; Patsourakos & Vourlidas 2011; Thompson et al. 2011), but its observations offer multiple interpretations. Such an event remains one of the most debated CMEs in the literature.

The Cartwheel CME is observed by the *SOHO*, *STEREO*, *Hinode*, and *TRACE* spacecraft and is associated with the active region 10989. Thompson et al. (2011) suggest that the CME followed another event and originated from the newly reformed filament after that initial eruption. From the observations, the CME does not follow a radial path in the low corona. The Cartwheel deflects southward in latitude (Landi et al. 2010; Savage et al. 2010; Patsourakos & Vourlidas 2011; Thompson et al. 2011) and inverts its motion at $\sim 2 R_{\odot}$ (Landi et al. 2010; Gui et al. 2011). Longitudinally, it seems the CME moves eastward and then westward (Landi et al. 2010; Patsourakos & Vourlidas 2011). Moreover, observations show that the CME rotates during its propagation outward (Patsourakos & Vourlidas 2011). This rotation pattern is discussed and modeled in Thompson et al. (2011): the flux rope seems to be twisting up to $4 R_{\odot}$, first counterclockwise ($\sim 115^{\circ}$ until $2.5 R_{\odot}$) and then backward $\sim 15^{\circ}$ up to $3.3 R_{\odot}$. The CME core rapidly accelerates in a span of ~ 2 – $3 R_{\odot}$ and reaches an average speed of 450 km s^{-1} at $\sim 5 R_{\odot}$ (Landi et al. 2010). Patsourakos & Vourlidas (2011) detect the typical three-part structure of the CME (bright front, dark cavity, and bright core) as the structure propagates outward. Using electron density measurements, Landi et al. (2010) estimate the CME mass to be between 1.8 and $4.0 \times 10^{14} \text{ g}$.

In this paper, we model the Cartwheel CME with ForeCAT to reproduce not only the observed deflection, but its rotation as well.

2. Observations

We use data from *SOHO* and *STEREO-A* (Landi et al. 2010) for the Cartwheel CME’s latitude (λ) and longitude (ϕ). In this coordinate system, the X axis is in the Sun–Earth direction, the Y axis points west and the Z axis points north. The latitude λ is

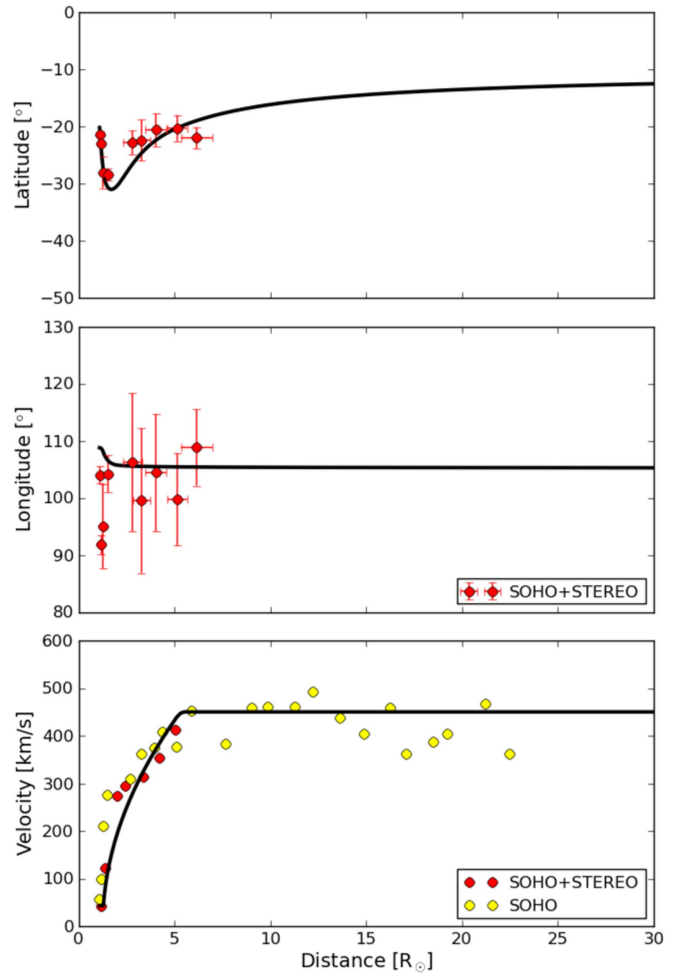


Figure 1. Cartwheel CME trajectory: latitude, longitude, and speed are plotted as a function of distance from the Sun in solar radii. The combined *SOHO* and *STEREO* observations are plotted in red and measurements from *SOHO* are in yellow. Data are from Landi et al. (2010). Error bars are associated only to latitude and longitude points. The best fit of ForeCAT ($\chi^2 = 8.9$) is displayed in black. For this specific output, the initial set of main parameters is in Table 1.

the elevation angle from the X – Y plane and the longitude ϕ is the angle on the X – Y plane, measured from the positive X axis. The plane Y – Z is the *SOHO* plane of sky.

Positions in the low corona (until $\sim 6 R_{\odot}$) are obtained in Landi et al. (2010) by combining simultaneous observations of the CME core detected by *SOHO* (EIT and LASCO instruments) and *STEREO-A* (EUVI, COR1, and COR2 instruments). Data in the low corona from *STEREO-B* cannot be used because, from its point of view, the CME is behind the Sun’s limb. In order to have the CME position, the reconstruction technique used in Landi et al. (2010) needs two viewpoints of the CME plasma. The CME core fades away in the *STEREO-A* COR 2A field of view beyond $6.2 R_{\odot}$; therefore, latitude and longitude data are not available after this point. Position measurements (and associated uncertainties) are shown as a function of distance from the Sun as red dots in Figure 1.

The error bars associated with these data points are smaller than what is generally assumed for CMEs using graduated cylindrical shell (GCS) fitting techniques ($\pm 5^{\circ}$ in latitude and $\pm 10^{\circ}$ in longitude, Thernisien et al. 2006, 2009) because they result from the image analysis itself (Landi et al. 2010) and are

directly related to the pixel size of the images. We account for this in Section 3 when comparing to simulations.

The observed latitudes show a complex trajectory: the flux rope deflects southward to almost -30° at $\sim 2 R_\odot$, then progressively moves northward to $\sim -20^\circ$ until $5-6 R_\odot$. The observed CME longitudes suggest that the CME deflects toward and away from Earth with radial distance (Figure 12 in Landi et al. 2010); however, the CME more likely keeps a constant longitude between 100° and 110° . In fact, the total uncertainty in the data points is likely larger than that obtained directly from the image analysis. Projection effects significantly affect longitude measurements, especially so close to the photosphere.

The bottom panel in Figure 1 shows the CME speed (red dots) as a function of solar distance. From the radial position measured with *SOHO* and *STEREO*, we calculate the radial speed of the CME as a first order time derivative. The yellow dots are the speed measurements (Landi et al. 2010) in the *SOHO* plane of the sky from 1.1 to $22.5 R_\odot$. These are obtained by extracting the speed from different CME positions in subsequent *SOHO*/LASCO images. The CME is ejected with a speed lower than 100 km s^{-1} , but progressively accelerates and maintains an overall constant velocity of 450 km s^{-1} after $\sim 5 R_\odot$.

3. Comparison with ForeCAT

ForeCAT simulations require several initial parameters. One set of parameters defines the CME shape. The CME flux rope is assumed to have a toroidal shape (Figure 2 in Kay et al. 2015b): a and c describe the height and width of the CME, b represents the thickness, and d is the center of the CME's toroidal axis above the surface of the Sun. Since the first data point in the Landi et al. (2010) *SOHO* and *STEREO*-A data set is so close to the Sun's surface ($R_0 = 1.1 R_\odot$), we consider the initial CME nose position to be $a + b + d = R_0$. We also set constraints on the initial shape parameters from Figure 6(a) in Thompson et al. (2011): we assume the distance between the two footpoints D as $D = 2c + 2b \sim 0.25 R_\odot$. These two equations are not a closed system; therefore, we end up with two free parameters that have to be fixed independently.

ForeCAT also requires the initial location of the CME in latitude and longitude. From Thompson et al. (2011; Figure 6a), the CME nose position is approximately at the midpoint of the two footpoints (-20.2° in latitude and 108.8° in longitude). The tilt of the CME is assumed to be $\theta = 50^\circ$ (angle between the meridian passing through the active region and the connecting line between the CME footpoints), but it is allowed to vary during the simulation because we include CME rotation in ForeCAT. The tilt matches the polarity inversion line orientation for the active region from which the Cartwheel CME is ejected.

Another important parameter is the CME initial mass, which we consider constant during the CME propagation (though works such as Kay et al. 2016 include an increasing CME mass due to plasma pile-up). Landi et al. (2010) give an estimate of the mass range between 1.8 and $4.0 \times 10^{14} \text{ g}$. We keep the CME mass as a free parameter and test whether the simulation outputs are consistent with the observed range.

An additional constraint is how a CME expands during its propagation. ForeCAT can use any CME expansion model described by an analytic function of radial distance. In this work, we focus on two types of expansion: a self-similar

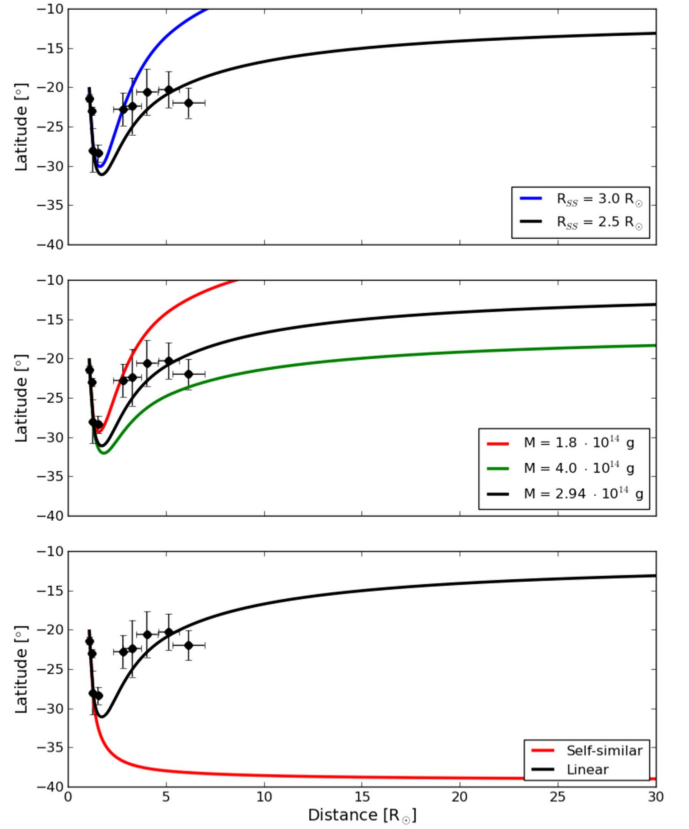


Figure 2. Sensitivity of the modeled ForeCAT latitude to R_{SS} (top), CME mass (middle), and expansion model (bottom). The observed data is shown with black points. The top panel shows the comparison with a magnetic background obtained by a PFSS model with a source surface radius of $R_{SS} = 2.5 R_\odot$ (black line) and $R_{SS} = 3.0 R_\odot$ (blue line). The middle panel compares masses: $M = 2.94 \times 10^{14} \text{ g}$ (black line), $M = 1.8 \times 10^{14} \text{ g}$ (red line), and $M = 4.0 \times 10^{14} \text{ g}$ (green line). The bottom panel shows ForeCAT sensitivity to expansion laws: linear angular width variation (black line) and constant angular width propagation (red line). The best fit shown in Figure 1 is displayed with a black line.

expansion model and a linear expansion model. The former assumes a constant angular CME width with radial distance, while the latter considers an angular width linearly increasing as the CME propagates outward. The relationship for the linear expansion model is

$$\alpha = m(R - 1) + k \quad (1)$$

where α is the angular width, m is the rate of change and k is the initial angular width at $R = 1 R_\odot$, and R is the radial distance. As the bottom panel in Figure 2 shows (see later in the section for details), a linear expansion model reproduces data significantly better than the self-similar expansion. The parameters m and k must be constrained for each CME case and are directly related to the initial shape parameters. α calculated at R_0 , in fact, they must match the one calculated geometrically as $\tan^{-1}\{(b+c)/d\}$. For the Cartwheel CME, since angular width data over radial distance are not provided, we cannot constrain m and k directly, but we consider how their variations affect the simulation outputs when compared to the available data (latitude, longitude, and speed). From the nose position of the CME and the footpoint separation, we can calculate $\alpha(R_0)$; therefore, we need to constrain only one parameter (either

Table 1
ForeCAT Initial Parameters for the Best Fit ($\chi^2 = 8.9$) in Figure 1

M [g]	a [R_\odot]	b [R_\odot]	c [R_\odot]	d [R_\odot]	lat_{in} [$^\circ$]	lon_{in} [$^\circ$]
2.94×10^{14}	0.0375	0.022	0.103	1.040	-20.19	108.76
θ [$^\circ$]	v_{in} [km s^{-1}]	v_{fin} [km s^{-1}]	m [$^\circ/R_\odot$]	k [$^\circ$]	R_{ga} [R_\odot]	R_{ap} [R_\odot]
50	43	450	24.2	4.4	1.3	5.3

Note. From the left to the right: mass, height, thickness, width, distance, latitude, longitude, tilt, initial speed, final speed, rate of angular width change, initial angular width, starting radial distance of acceleration, and ending radial distance of acceleration.

m or k). The remaining parameter is directly obtained from Equation (1) at R_0 .

ForeCAT initial parameters also require the CME speed. ForeCAT considers a three-phase propagation as described in Zhang & Dere (2006; Kay et al. 2013): the CME first gradually rises (from R_{ga} on speed is constant), then accelerates impulsively for a radial distance interval (between R_{ga} and R_{ap}) and lastly propagates at a constant speed (from R_{ap} on). The radial distances of each phase are treated as free parameters, but the Cartwheel CME data allow us to constrain the initial v_{in} and final v_{fin} speed, respectively, to 43 km s^{-1} (first speed data point) and 450 km s^{-1} (average of the speed data points after $7 R_\odot$).

As mentioned, we can fully data-constrain only part of the ForeCAT set of initial parameters (nose position, initial and final speed). We use a random walk test to determine the rest (shape parameters, mass, initial angular width at the Sun's surface, angular width rate of change, radial distances for the three-phase propagation). To start the analysis, we specify a potential range for each of the unknown ForeCAT inputs. The test then involves performing a random walk selecting new values for each parameter and running a ForeCAT simulation. The new parameters are either accepted or rejected based on a comparison between the match of ForeCAT results to observations and that of the previous step. The random walk test runs until the χ^2 is less than 1 or the number of iterations requested is reached (generally high enough that the parameters do not cause a significant change in the χ^2 anymore). Out of this process, we select the initial parameter set with the lowest χ^2 .

Figure 1 displays the comparison between data and the ForeCAT simulation. The model output (black line) in Figure 1 corresponds to the best fit ($\chi^2 = 8.9$). The lowest χ^2 is obtained with the set of parameters in Table 1.

From the top panel, the simulation clearly matches the latitude data within the error bars: the CME deflects 10° southward and deflects back northward to -20° . ForeCAT provides a good match within the error bars for the longitude data as well (middle panel); however, we cannot reproduce the observed initial position. Close to the Sun's surface, it is difficult to correctly measure longitude due to projection effects. The errors given from the image analysis likely underrepresent the full uncertainty in the measured position. It is indeed very unlikely that the CME would deflect so much in longitude in such a short time.

In the bottom panel of Figure 1, we show the velocity as a function of radial distance. The ForeCAT simulation shows that the CME propagates at a constant speed of 43 km s^{-1} until $1.3 R_\odot$, accelerates between $1.3 R_\odot$ and $5.3 R_\odot$, and propagates outward at 450 km s^{-1} . The distance intervals of uniform speed and acceleration are obtained from the random walk test. There

is an overall agreement between the data points and the simulation, especially in the low corona, where the CME position deflection mainly occurs.

In order to match the trajectory in latitude, we had to include a velocity component in the latitudinal direction of -42 km s^{-1} . This extra non-radial component is negative, since the CME is moving southward initially. The combination of the radial and latitudinal components matches the first data point of the plane of sky speed ($\sim 60 \text{ km s}^{-1}$) in *SOHO* measurements.

The best fit in Figure 1 constrains the CME expansion model in the low corona as well. The CME's angular width linearly expands as described in Equation (1), with $m = 24.2/R_\odot$ and $k = 4.4^\circ$. From the random walk test, besides m and k , we also constrain that the CME instead self-similarly expands from $2.1 R_\odot$ outward.

The CME is allowed to rotate in all the simulations run for this work. The best fit gives a rotation of only $\sim 12^\circ$. This small effect clearly shows that magnetic background forces calculated from a static magnetic background are not strong enough to cause the observed rotation from the images (Thompson et al. 2011), which may result from dynamic changes like reconnection events, not included in the model.

Figure 2 shows the sensitivity of ForeCAT to different initial parameters: we compare the best fit (black line) to those obtained varying only one parameter in the set (colored lines). We explored the sensitivity for the source surface radius R_{SS} , the mass M , and the expansion laws, focusing solely on the latitudinal deflection.

The curve with $R_{\text{SS}} = 2.5 R_\odot$ is in black and the one with $R_{\text{SS}} = 3.0 R_\odot$ is in blue. One can see that the CME is highly sensitive to the magnetic background as a change of $0.5 R_\odot$ causes the flux rope to be pushed north much quicker. The magnetic field used in the blue trajectory, in fact, has closed field lines until $R_{\text{SS}} = 3.0 R_\odot$; therefore, the resulting magnetic forces until that distance are stronger and cause more deflection. However, it is possible to obtain a good fit for a $R_{\text{SS}} \neq 2.5 R_\odot$, granted that the other parameters involving the expansion (shape parameters and m and k) are correctly changed as well.

Next, we explored the sensitivity to the CME initial mass (middle panel), within the limits obtained by Landi et al. (2010). As expected, a massive CME ($M = 4.0 \times 10^{14} \text{ g}$, green line) will be affected less by magnetic forces contrary to a lighter CME ($M = 1.8 \times 10^{14} \text{ g}$, red line) for which the trajectory can be more easily changed. Both of these masses result in simulations that reproduce the initial southward deflection, but fail to reproduce the latitudinal reversal correctly.

The bottom panel compares the linear expansion to the self-similar one. The red line shows the simulation with a constant

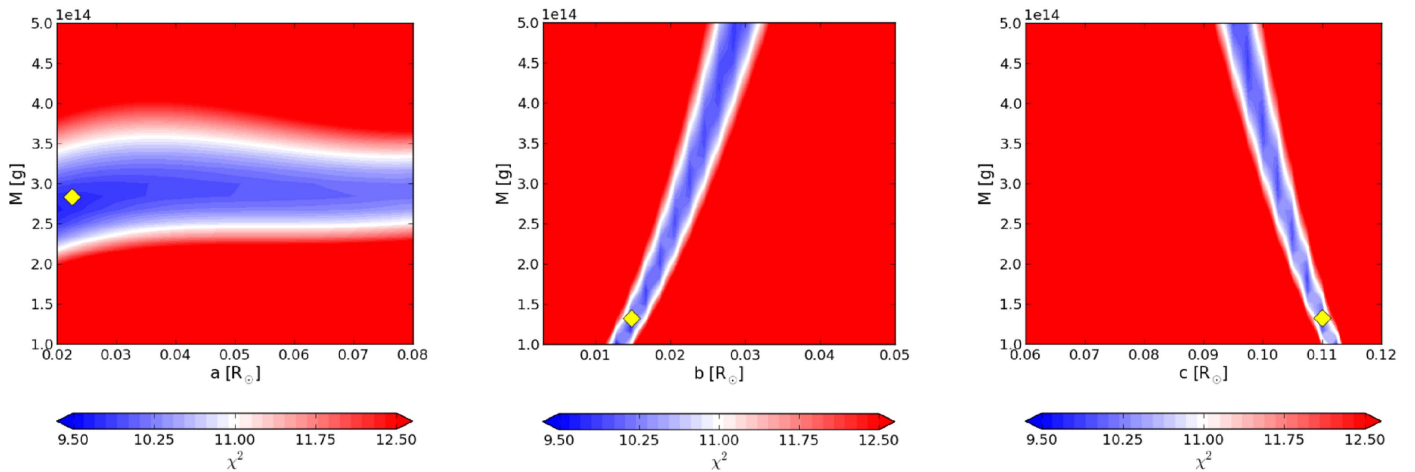


Figure 3. Test of χ^2 between the initial CME mass M and the shape parameters a (left plot), b (middle plot), and c (right plot) performed on latitude data only. The contour colors represent χ^2 values and the white color represents where $\chi^2 \sim 11$. The only parameters varying in the left plot are M , a , and, as a result, d . For the central plot, the free parameters are M , b , c , and d from $D = 2c + 2b \sim 0.25 R_\odot$ and $a + b + d = R_0 = 1.1 R_\odot$. The plot on the right has M , c , b , and d varying. The initial angular width varies accordingly. The yellow diamonds represent the lowest χ^2 values for the test performed. For M vs. a , the lowest χ^2 is 9.7, corresponding to $M = 2.83 \times 10^{14}$ g and $a = 0.022 R_\odot$. For M vs. b , the lowest χ^2 is 9.8, corresponding to $M = 1.33 \times 10^{14}$ g and $b = 0.015 R_\odot$. For M vs. c , the lowest χ^2 is 9.7, corresponding to $M = 1.33 \times 10^{14}$ g and $c = 0.11 R_\odot$.

angular width of $\alpha = 6^\circ.8$, which is the angular width of the CME, corresponding to the best fit shown in Figure 1. Keeping the angular width constant during the CME propagation would cause a southern deflection with no reversal back to lower latitude values, causing a mismatch with data after $1.54 R_\odot$, no matter the initial angular width value used.

To better understand the model’s sensitivity to the initial CME geometry, rather than displaying single simulation outputs, we performed a reduced χ^2 test with the latitude data only, varying the mass and the shape parameters a , b , and c . All of the other parameters are kept fixed as in Figure 1, and the initial shape parameters and the initial angular width are kept consistent with each other; the relationship between the footpoint separation ($D = 2c + 2b \sim 0.25 R_\odot$) and nose position ($R_0 = 1.1 R_\odot$) is also maintained. Unlike the random walk test in which all parameters are varied simultaneously, we select a range for only two parameters, run ForeCAT for 625 simulations covering this range (25 sub-intervals in each parameter), and calculate the χ^2 for each one.

Figure 3 shows the results of this sensitivity study: the colorbar indicates the χ^2 values, the y-axis represents the mass range and the x-axis is the parameter a for the plot on the left, b for the middle plot, and c for the plot on the right. Given the small uncertainties for the data considered, the χ^2 never approaches unity, but we can consider the regions of lowest χ^2 and assume them to constrain the parameters. χ^2 values lower than 11 correspond to good fits, which are displayed in blue in all three plots. The yellow diamond in each plot represents the lowest χ^2 for that specific parameter space, which is 9.7 for the left and right plots and 9.8 for the middle one.

Considering the regions where the χ^2 is lower than 11, we can constrain the initial mass and the shape parameters of the CME. The good χ^2 for M and a corresponds to a mass range of $2.3 - 3.0 \times 10^{14}$ g, which is within the range provided by Landi et al. (2010). In this mass range, the lowest χ^2 for b is 9.9 and it corresponds to $M = 2.5 \times 10^{14}$ g and $b = 0.021 R_\odot$. Similarly, the lowest χ^2 for c is 9.9, corresponding to $M = 2.3 \times 10^{14}$ g and $c = 0.105 R_\odot$. By combining the middle and left plot to satisfy the footpoint separation and focusing on only the mass range of $(2.3 - 3.0) \times 10^{14}$ g, the

values for b and c are, respectively, $0.02 R_\odot$ and $0.10 R_\odot$. We cannot constrain a within the range considered ($0.02 - 0.08 R_\odot$) and the sensitivity study gives a range for d of $1.00 - 1.06 R_\odot$. These values correspond to shape ratios of $A = a/c = 0.2 - 0.8$ and $B = b/c = 0.2$ and resemble a squat ($A < 1$) and thin ($B < 1$) CME.

4. Summary and Discussion

In this work, we have analyzed the 2008 April 9 CME, known as the “Cartwheel CME.” This event was not geomagnetically significant because it did not reach Earth’s magnetosphere, but it offers an interesting case to test its low corona deflection. Images from *STEREO* and *SOHO* clearly display a rotation of the structure in the low corona and a reversal in its original latitude direction: the CME moves southward at first and changes its direction toward north at $\sim 1.50 R_\odot$.

Within the uncertainties, the CME trajectory in the low corona (until $\sim 5 R_\odot$) can be reproduced by the ForeCAT model as showed in Figure 1. The modeled CME trajectory shown is the best fit ($\chi^2 = 8.9$) and is obtained with the set of parameters in Table 1. The model successfully traces the reversal in latitude direction and the CME speed profile. Longitude data is also well approximated, except for the very first points, where projection effects might have affected the measurements.

Our paper also shows that ForeCAT is sensitive to parameter changes, such as the initial mass, the expansion model and the initial shape parameters. Moreover, being a magnetic forces-based model, the CME trajectory is significantly affected when we introduce a variation of the magnetic background by changing the source surface radius.

Figure 2 shows examples of how ForeCAT’s outputs vary when changing only one parameter at the time. The most significant result is obtained when the expansion for the CME is switched from a linear one to a self-similar model that assumes a constant angular width: the simulation fails to reproduce data in the latter case, clearly showing that a simplistic expansion is not correct in the lower corona. After

2.1 R_{\odot} , instead, assuming a constant angular width is a good approximation that matches the data. The constraint we are able to put on the CME expansion is important also when modeling CME propagation with MHD simulations. In MHD models, indeed, since the CME is often initiated in a non-equilibrium state, it tends to over-expand in the low corona.

Our sensitivity study also confirms that the Landi et al. (2010) mass limits are reasonable and shows that we can further constrain the mass. In Figure 3, if we overlap the parameter space regions of $\chi^2 \leq 11$ in each subplot, we manage to constrain the mass to a narrow band of $(2.3\text{--}3.0) \times 10^{14}$ g that is well within the Landi et al. (2010) mass range.

As Figure 3 shows, ForeCAT is more sensitive to b and c rather than a : the parameter space of regions of lowest χ^2 are much smaller for the comparison of M versus b and M versus c parameter space rather than M versus a . The parameters b and c still match the distance between the footpoints, but give further information on the CME initial shape: the radius of the flux rope (b essentially) is much smaller than the non-radial extension of the CME (c). On the other hand, the parameter a does not significantly affect the results, mainly because the initial nose position of the CME is fixed in space ($R_0 = 1.1 R_{\odot}$). Generally, variations of a combined with a varying nose position surely determine different trajectories and select a smaller region in the χ^2 map. The magnetic forces resulting from magnetic gradients, in fact, vary significantly in the radial direction, especially close to the Sun's surface. Therefore, placing the CME nose closer to or further away from the photosphere affects its trajectory besides its shape. Our study, however, is focused on the effect that shape parameters alone might have on the CME trajectory rather than its position, since we have the initial height and location of the CME from observations.

Similar to the mass constraint, if we overlap the parameter space regions of $\chi^2 \leq 11$ in each subplot, we find values of $0.02 R_{\odot}$ and $0.10 R_{\odot}$ for b and c , respectively. For the shape parameter a , instead, we cannot constrain further than the range analyzed ($0.02\text{--}0.08 R_{\odot}$), which proves that ForeCAT is not very sensitive to the radial elongation of the CME when the nose position is fixed.

Errors associated with the latitude and longitude data points are obtained directly from the image analysis itself, and therefore represent the uncertainty in the technique itself rather than the uncertainty inherent in the position reconstruction. These errors are in fact lower than the usual uncertainties on the latitude and the longitude (respectively $\pm 5^\circ$ and $\pm 10^\circ$) when one uses the GCS reconstruction technique, causing χ^2 to never reach unity. If the same analysis is performed with the $\pm 5^\circ$ GCS latitude uncertainties, χ^2 can easily get to 1, but since this uniformly decreases the χ^2 value throughout parameter space, the best fit is still found in the same regions of Figure 3.

The peculiarity of this CME definitely lives in the reversal in latitudinal deflection, very different than previous CME successfully matched by ForeCAT (Kay et al. 2015a, 2016, 2017). We show in this work how ForeCAT can still reproduce the complex CME trajectory after taking into account magnetic tension and magnetic forces only, if we include an appropriate initial non-radial velocity and a linear angular width expansion law.

The initial velocity of the CME is non-radial because of the latitudinal component of -42 km s^{-1} we had to include to match latitude data. Unlike previous cases analyzed with

ForeCAT, having such a non-zero component is necessary for this CME. We can justify such an assumption if we invoke an asymmetric magnetic reconnection event (see Murphy & Lukin 2015 and Su & van Ballegooijen 2013). If the magnetic reconnection that initiates the CME is asymmetrical with respect to the footpoints, the CME would be ejected non-radially. For the first part of its trajectory, in fact, the CME moves south against the magnetic gradients. The magnetic forces progressively slow down the CME from moving southward until a reversal point is reached at $\sim 2 R_{\odot}$ and the CME is pushed back north, toward the HCS, as discussed in previous works (Kay et al. 2013, 2015b, 2016).

Despite including rotation in the model, the CME rotates less than $\sim 12^\circ$ for the specific set of parameters in Figure 1, much less than what is observed (counterclockwise rotation of $\sim 115^\circ$ until $2.5 R_{\odot}$ and backward rotation of $\sim 15^\circ$ up to $3.3 R_{\odot}$ —Thompson et al. 2011). Such a significant observed rotation might be an additional observational signature that an asymmetric magnetic reconnection process occurred during the ejection, which could initiate a CME rotation much more effectively than a torque produced by the background solar wind magnetic forces.

The solar magnetic field in ForeCAT is reconstructed from a synoptic magnetogram, but the model does not account for any time variations of it. Using a static magnetic background implicitly assumes the CME timescales are much faster than those in which the solar magnetic field varies. This approximation is more applicable for a solar minimum case than a solar maximum period, but it is still not very realistic, especially in the very early stages of the CME ejection. At this time, in fact, dynamic processes might affect the initial conditions of the ejection or early propagation so much that it is impossible to account for them from a static magnetic background. The Cartwheel CME is a clear example where dynamic processes need to be considered.

In summary, ForeCAT not only reproduces the results of experimental observations, but also helps in constraining the CME mass, shape, and expansion. Our analysis, in addition, hints at a possible asymmetric reconnection process occurring at the CME ejection, which could justify the significant rotation and the peculiar deflection of the Cartwheel CME.

References

- Byrne, J. P., Maloney, S. A., McAteer, R. T. J., et al. 2010, *NatCo*, **1**, 74
- Cremades, H., & Bothmer, V. 2004, *A&A*, **422**, 307
- Gopalswamy, N., Mäkelä, P., Xie, H., et al. 2009a, *JGR*, **114**, A00A22
- Gopalswamy, N., Yashiro, S., Michalek, G., et al. 2009b, *EM&P*, **104**, 295
- Gosling, J. T. 1993, *JGR*, **98**, 18937
- Gosling, J. T., McComas, D. J., Phillips, L., et al. 1991, *JGR*, **96**, 7831
- Green, L. M., Kliem, B., Török, T., et al. 2007, *SoPh*, **246**, 365
- Gui, B., Shen, C., Wang, Y., et al. 2011, *SoPh*, **271**, 111
- Hildner, E. 1977, in *Study of Travelling Interplanetary Phenomena*, Vol. 71, ed. M. A. Shea, D. F. Smart, & S. T. Wu (Dordrecht: D. Reidel), 3
- Isavnin, A., Vourlidas, A., & Kilpua, E. K. J. 2014, *SoPh*, **289**, 2141
- Kay, C., dos Santos, L. F. G., & Opher, M. 2015a, *ApJL*, **801**, L21
- Kay, C., Gopalswamy, N., Reinard, A., et al. 2017, *ApJ*, **835**, 117
- Kay, C., Opher, M., Colaninno, R. C., et al. 2016, *ApJ*, **827**, 70
- Kay, C., Opher, M., & Evans, R. M. 2013, *ApJ*, **775**, 5
- Kay, C., Opher, M., & Evans, R. M. 2015b, *ApJ*, **805**, 168
- Kilpua, E. K. J., Pomoell, J., Vourlidas, A., et al. 2009, *AnGeo*, **27**, 4491
- Kliem, B., Török, T., & Thompson, W. T. 2012, *SoPh*, **281**, 137
- Landi, E., Raymond, J. C., Miralles, M. P., et al. 2010, *ApJ*, **711**, 75
- Luhmann, J. G., Li, Y., Arge, C. N., et al. 2002, *JGR*, **107**, 1154
- Lynch, B. J., Antiochos, S. K., Li, Y., et al. 2009, *ApJ*, **697**, 1918

- MacQueen, R. M., Hundhausen, A. J., & Conover, C. W. 1986, [JGR](#), **91**, A1
- Mays, M. L., Thompson, B. J., Jian, L. K., et al. 2015, [ApJ](#), **812**, 2
- Möstl, C., Amla, K., Hall, J. R., et al. 2015, [ApJ](#), **787**, 119
- Murphy, N. A., & Lukin, V. S. 2015, [ApJ](#), **805**, 134
- Patsourakos, S., & Vourlidas, A. 2011, [A&A](#), **525**, A27
- Savage, S. L., McKenzie, D. E., Reeves, K. K., et al. 2010, [ApJ](#), **722**, 329
- Shen, C., Wang, Y., Gui, B., et al. 2011, [SoPh](#), **269**, 389
- Su, Y., & van Ballegoijen, A. 2013, [ApJ](#), **764**, 91
- Thernisien, A., Howard, R. A., & Vourlidas, A. 2006, [ApJ](#), **652**, 763
- Thernisien, A., Vourlidas, A., & Howard, R. A. 2009, [SoPh](#), **256**, 111
- Thompson, W. T., Kliem, B., & Török, T. 2011, [SoPh](#), **276**, 241
- Thompson, W. T., Kliem, B., & Török, T. 2012, [SoPh](#), **276**, 242
- Vourlidas, A., Colaninno, R., Nieves-Chinchilla, T., et al. 2011, [ApJL](#), **733**, L23
- Zhang, J., & Dere, K. P. 2006, [ApJ](#), **649**, 1100
- Zhao, X., & Hoeksema, J. T. 1995, [JGR](#), **100**, A1